Reduced-Order Kinetic Monte Carlo Model to Simulate Water Diffusion in Biodegradable Polymers

Jesse M. Sestito[a,b], Tequila A. L. Harris[a+], Yan Wang[a]*

[a]Woodruff School of Mechanical Engineering, Georgia Institute of Technology, 813 Ferst Drive NW, Atlanta, GA 30332, USA

[b]College of Engineering, Valparaiso University, 1900 Chapel Drive, Valparaiso, IN 46383, USA

*Email: yan-wang@gatech.edu. Phone: +1 404 8944714. Fax: +1 404 8949342.

+Email: tequila.harris@me.gatech.edu. Phone: +1 404 3856335. Fax: +1 404 8949342.

Abstract

Water is a driving factor in the degradation process of biodegradable polymers. However, water diffusion is typically not incorporated in the kinetic models of biodegradation such as kinetic Monte Carlo (kMC), because water diffusion events occur at a much shorter time scale than the hydrolysis reactions. As such, there is a need to improve the computational efficiency of water diffusion in the kMC models of diffusion processes in biodegradation. In this work, a new dimensionality reduction scheme for kMC diffusion models is developed to significantly reduce the computation time, where a two-dimensional kMC diffusion model for porous microstructures is reduced to one-dimensional ones. The dimensionality reduction is accomplished by calibrating the model parameters with multi-objective Bayesian optimization. The reduced-order diffusion model shows a 675-fold faster computation compared to the original two-dimensional model.

Graphical Abstract
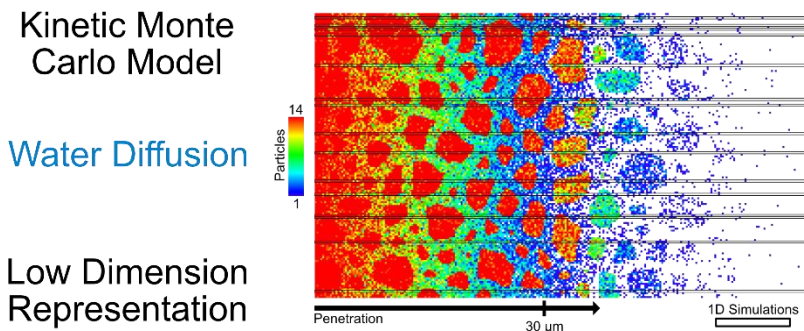
Keywords

Kinetic Monte Carlo; Dimensionality reduction; Water diffusion; Biodegradable polymeric scaffold

1   Introduction

Biodegradable polymers have been used to construct scaffolds which are implanted into the human body to support tissue regrowth and to regenerate the mechanical structure in a region [1]. For scaffold design, it is important to understand how different scaffolds degrade over time so that the structures and materials can be customized for different needs of patients. *In vitro* and *in vivo* experiments can be costly and time consuming. As such, computational models have been utilized to examine the impacts of physiological conditions on the biodegradation processes such as hydrolysis reaction [2–7] and water diffusion [5,8], as well as predictions of degraded mechanical properties over time [9]. Particularly, Monte

Carlo modeling has been used to simulate the overall biodegradation process [10–12]. However, the details of reactions and diffusions were not predicted. Kinetic Monte Carlo (kMC) has been used to simulate detailed biodegradation processes including hydrolysis reaction, bulk erosion, oligomer diffusion, and crystallization [3,13,14]. However, those kMC models have not incorporated water diffusion, which is a key component in biodegradation.

kMC has been applied to simulate the diffusion of atoms or particles as hops between different lattice sites. The rate of diffusion depends on the activation energy that is necessary for the hops [15–17]. The activation energy can be estimated from either first-principles calculations or experimental measurements. kMC can also be used to simulate the large-scale systems efficiently when the particles are molecules or larger units instead of atoms, such as the diffusion of CH_4 molecules in water [18], cell migration in 3D biomaterials [19], and water adsorption [20]. The main advantage of kMC diffusion models is that the computational cost is only determined by the number of events and is independent from the length scale of the simulated system. Therefore, large systems can be simulated efficiently with the properly defined event catalog. The second advantage is that the simulation can provide fine-grained details even in a large domain. However, in the kMC diffusion models, diffusion is the sole event that occurs without other types of events such as reaction because the timescale disparities between the diffusion and reaction events will make kMC computationally inefficient.

One challenge of simulating the water diffusion in biodegradation with kMC is that the diffusion rate can be several magnitudes higher than the ones of reaction and phase transition. If reaction and diffusion are combined into one kMC model, most of the computational time and resources will be spent on diffusion, since the computational time in kMC depends on the number of events that occur. Research efforts of incorporating events of different timescales in kMC have been made. For instance, kMC can be run in parallel with continuous-time simulations in solving partial differential equations for longer timescale [21–24]. Statistical averaging can be applied to wait for fast dynamics to come to a quasi-equilibrium before the slow dynamics take effect [25]. In the τ-leap method, a number of events can occur simultaneously to advance the simulation [26,27]. Events can also be clustered based on their speeds and the simulation is run in a nested loop [28,29]. Another approach to accelerate kMC is through coarse-graining methods [30,31], where a collection of molecules is modeled as a single particle. The effective events that occur are then assigned to the single particle, which reduces a collection of events to a single event. Adaptive coarse-grained Monte Carlo simulation can be taken where a finer grid is used in high-fidelity zones while the coarser one is applied in other domains [32]. The idea of coarse-graining has also been further extended to combining different types of events [33].

In this research, a dimensionality reduction technique for kMC is developed to accelerate diffusion simulations, which significantly reduces the overall number of events. This is accomplished by reducing a high-dimensional simulation model to multiple lower-dimensional ones, and the low-dimensional results are combined to approximate the original model. In this work, a two-dimensional (2D) simulation is reduced to multiple 1D simulations, where the rates for the 1D simulations are calibrated based on the 2D simulation. The calibration is performed using a multi-objective Bayesian optimization (MOBO) approach. The 1D reduced-order models are applied to examine water diffusion in a 2D polycaprolactone (PCL) structure, where microscopic pores exist. The results show that the reduced-order models can effectively predict the diffusion in porous materials. In the remainder of the paper, the method to create the reduced-order kMC models is described in Section 2, where a Potts model is used to generate porous microstructures of PCL and the diffusion rates are calibrated with MOBO. The simulation results are shown in Section 3.

2 Methodology

To generate the porous microstructures in polymeric materials, a Potts model is first developed. The diffusion rates in the 2D kMC model are then estimated and calibrated from experimental measurements, whereas the rates in the 1D reduced-order models are calibrated based on the 2D model.

2.1 Porous Structure Generation

It is important to generate accurate microstructures of PCL with pores for water diffusion simulation. It has been shown that PCL is mostly composed of micrometer-scale pores that are spherical or elliptical in shape with low interconnectivity [34–37]. The porosity and pore sizes inside the structure vary greatly depending on the manufacturing method. Abedalwafa *et al.* reported a porosity of 43% of PCL [38], whereas PCL scaffolds can be made with a porosity of 66% and average pore size of 24 μm when manufactured using thermally induced phase separation [36], a porosity of 67.5% and average pore size of 2 μm when cast into thin films [39], or a porosity of 78% and average pore size of 2.8 ± 1.2 μm when 3-D printed [34]. The porosity can range from 46 to 85% by making small changes in the phase inversion and salt leaching manufacturing process [35]. Therefore, the generated microstructures in this work will have a porosity in the range of 45 to 55% with an average pore diameter of about 3 μm.

The PCL microstructures are generated based on the Potts model. The model is not to simulate the process of phase formation and growth. Rather it is to generate the 2D grain alike microstructures in PCL with micropores. As shown in Figure 1 (a), the pores are treated as grains and grow in the 2D domain. Post-processing is then applied to generate the 2D PCL network from the grain boundaries. In post-processing, morphological operations including edge finding, edge growth, scaling, and pore smoothing are applied to the pixel-based structure model. First, the edges are detected using a Sobel filter along both 2D axes. This produces two distinct pixel values, edges for the PCL network and pores everywhere else, as shown in Figure 1 (b). The edges are then grown by iteratively changing all voxels directly adjacent to a structure pixel to a structure pixel. This process is repeated until a desired porosity is achieved as illustrated in Figure 1 (c). Finally, the sharp edges are smoothed by upsampling, blurring, and downsampling. An example of the final structure is shown in Figure 1 (d).

Porosity ρ for the 2D structure is calculated as the number of pore pixels (n_{pv}) per the total number of pixels. The edge growth step is repeated until a desired ρ is obtained. The average area of a pore $\bar{A}_{pore}$ can be obtained from counting n_{pv} and the number of pores n_p within a region, as

$$\bar{A}_{pore} = \frac{n_{pv}}{n_p} = \pi \left(\frac{\bar{d}_{pore}}{2} \right)^2 \tag{1}$$

where $\bar{d}_{pore}$ is equivalent average pore diameter. The image can also be scaled by a scaling factor (S) to obtain the desired average pore diameter ($\bar{d}_{pore}^{(d)}$) as

$$\bar{d}_{pore}^{(d)} = S\bar{d}_{pore} \, . \tag{2}$$

The scale factor can also be applied to the image to produce a structure with a specified pore size and desired porosity.
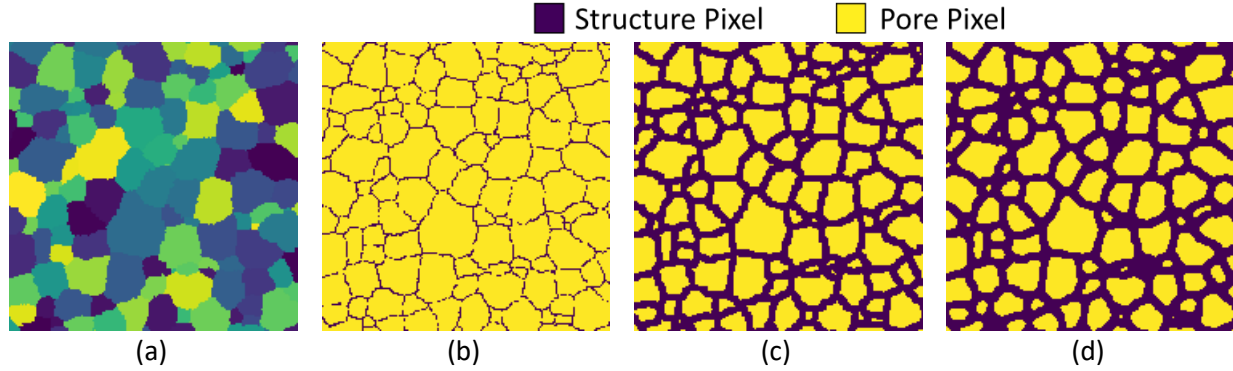
| (a) | (b) | (c) | (d) |

Figure 1. The steps used in the generation of a 2D porous PCL microstructures. (a) Pore formation from the Potts model, (b) edge detection, (c) edge growth, (d) and pore smoothing to generate the final structure.

2.2   Diffusion Rates for kMC

Here, a formal approach to estimate the water diffusion rate is developed for the kMC simulations. For the diffusion of water through a bulk polymer, the diffusion rate (R_D) at which water leaves a volumetric domain is dependent on the molecular weight (Mn) of the material, the number of water molecules (n_W) in the domain, the volume of the domain (V), and the diffusion coefficient (D).

The rates in kMC can be generally defined statistically using the first passage time [40,41]. The first passage time (t_{fp}) is the average time it takes for an event to occur [42,43]. The first passage time for a water molecule exits a domain in diffusion is estimated from the diffusion model

$$\frac{\partial C}{\partial t} = D\left(\frac{\partial^2 C}{\partial x^2} + \frac{\partial^2 C}{\partial y^2} + \frac{\partial^2 C}{\partial z^2}\right) \tag{3}$$

for a constant diffusion coefficient D, where C is concentration of water or the probability of finding the water molecule at a particular location at time t as probability density function (PDF) [44]. Equation (3) can be solved with path integral based on Green's function [45]

$$G(\boldsymbol{r}, \boldsymbol{r_0}, \tau) = \frac{1}{(4\pi D\tau)^{\frac{3}{2}}} e^{-\frac{|\boldsymbol{r}-\boldsymbol{r_0}|^2}{4D\tau}} \tag{4}$$

where $\boldsymbol{r} = (x, y, z)$ is the new location and $\boldsymbol{r_0}$ is the original location of the water molecule in Euclidean space for a time period τ [44]. The probability that a water molecule diffuses away from the origin with at least the distance r_b during the time period τ is

$$P(|\boldsymbol{r}| > r_b|\tau) = \int_{r_b}^{\infty} G(\boldsymbol{r}, \boldsymbol{0}, \tau)d\boldsymbol{r} = \int_{r_b}^{\infty} \frac{1}{(4\pi D\tau)^{\frac{3}{2}}} e^{-\frac{|\boldsymbol{r}|^2}{4D\tau}} d\boldsymbol{r}$$
$$= 1 - \int_{\boldsymbol{0}}^{r_b} \frac{1}{(4\pi D\tau)^{\frac{3}{2}}} e^{-\frac{|\boldsymbol{r}|^2}{4D\tau}} d\boldsymbol{r} \tag{5}$$

where $\boldsymbol{r_b}$ is the vector in the domain bounded by r_b.

For a particle that travels out of a three-dimensional cube with length l, Equation (5) becomes

4

$$P\left(|x|>\frac{l}{2} \text{ or } |y|>\frac{l}{2} \text{ or } |z|>\frac{l}{2}\Big|\tau\right) = 1 - \int_{-\frac{l}{2}}^{\frac{l}{2}}\int_{-\frac{l}{2}}^{\frac{l}{2}}\int_{-\frac{l}{2}}^{\frac{l}{2}} \frac{1}{(4\pi D\tau)^{\frac{3}{2}}} e^{-\frac{(x^2+y^2+z^2)}{4D\tau}} \, dx \, dy \, dz. \tag{6}$$

Equation (*6*) can be rewritten due to symmetry as

$$P\left(|x|>\frac{l}{2} \text{ or } |y|>\frac{l}{2} \text{ or } |z|>\frac{l}{2}\Big|\tau\right) = 1 - \frac{8}{(4\pi D\tau)^{\frac{3}{2}}}\int_{0}^{\frac{l}{2}}\int_{0}^{\frac{l}{2}}\int_{0}^{\frac{l}{2}} e^{-\frac{(x^2+y^2+z^2)}{4D\tau}} \, dx \, dy \, dz \tag{7}$$

where τ and D are assumed constant. Equation (*7*) can be solved using computational methods. The probability that the travel time T is less than τ for a water molecule reaches the boundary can be established from equation (*7*), as

$$F_T(t) = P(T \leq \tau) = P\left(|x|>\frac{l}{2} \text{ or } |y|>\frac{l}{2} \text{ or } |z|>\frac{l}{2}\Big|\tau\right) \tag{8}$$

To calculate the first passage time (t_{fp}), which is the average amount of time required for the particle diffuses out of the domain, equation (8) is set equal to 0.5 such that there is a 50% chance the particle will have left the cube such that

$$F_T(t_{fp}) - 0.5 = 0. \tag{9}$$

Given the values of D and l, t_{fp} can be obtained by solving Equation (9) with root finding methods. Assuming there is an equal probability that the water molecule leaves the cube from any of the six sides, the diffusion rate is then given by

$$R_{D,1} = \frac{1}{6t_{fp}}. \tag{10}$$

This rate can then be multiplied by the number of water molecules, w, in the domain to receive the final overall rate of diffusion

$$R_{D,w} = w\,R_{D,1}. \tag{11}$$

However, solving Equation (9) for the cubic domain based on Equation (6) is computationally expensive. A simplification is to approximate with a spherical domain of radius r_v. Equation (*5*) becomes

$$P(r > r_v \mid \tau) = 1 - \int_0^{r_v} \frac{1}{(4\pi D\tau)^{\frac{3}{2}}} e^{-\frac{r^2}{4D\tau}} (4\pi r^2) \, dr, \tag{12}$$

where r is magnitude of the distance the particle has traveled in Euclidean space. Equation (12) can be simplified analytically as

$$P(r > r_v \mid \tau) = \text{erfc}\left(\frac{r_v}{2\sqrt{D\tau}}\right) + \frac{r_v e^{\frac{-r_v^2}{4D\tau}}}{\sqrt{\pi D\tau}} \tag{13}$$

where

$$\text{erfc}(x) = \frac{2}{\sqrt{\pi}}\int_x^{\infty} e^{-t^2} \, dt. \tag{14}$$

The first passage time t_{fp} can now be obtained by solving Equation (9).

The calculated R_D for a spherical domain needs to be further converted to one that is equivalent to a cubic domain. Since the rates are calculated based on volumes, the equivalent volumes are used, where

$$r_v = l \left(\frac{3}{4\pi} \right)^{\frac{1}{3}}. \tag{15}$$

The developed method to estimate the water diffusion rates for kMC, without consideration of the physical driving force such as interfacial tensions, only works for homogeneous solid structures. For pores represented as void cubic domains or voxels, water preferentially diffuses out of hydrophobic materials such as PCL and accumulates in the pores [46]. That is, water prefers to fill and saturate pores inside the material [47]. To adjust the water diffusion rates for saturation, modifications can be made empirically to the water diffusion rate by considering the interactions of pores and their neighbors. For instance, the water diffusion rate at which water enters a pore voxel from a structure voxel is increased by about four times based on experimental observation [47]. Further, to minimize the computational burden caused by the event that water diffuses between two neighboring pore voxels the rate can be reduced by about 20 times the largest structure diffusion rate. This is to reduce the number of those events that occur in the simulation so that the water would rather remain within the pore. This 20 times reduction does not make a difference for the final kMC result. The initial rate is empirically calibrated based on the statistical average of the number of water molecules within the pore [48]. The interfacial tension of the water drives water to enter the pores and to encourage pore saturation. As such, the rate at which a water molecule leaves a pore voxel and enters a structure voxel is eight times less likely than the pore-to-pore diffusion rate. The adjustment of these rates needs to avoid significant increases in the number of kMC events, which would be computationally expensive.

The water diffusion rates for the kMC simulation must be calibrated. Equation (*3*) allows for the calculation of the time, t, for the water molecules to travel a theoretical mean penetration distance, $\overline{m}_t$, in the bulk material. Assuming 1D flow of fluid and no water molecules initially in the material, $\overline{m}_t$ is given by

$$\overline{m}_t = \sqrt{2tD}. \tag{16}$$

The water diffusion rate in Equation (11) can then be adjusted with a scaling factor k_{bulk} as

$$R'_{D,w} = k_{bulk} \times R_{D,w} \tag{17}$$

such that the mean water penetration distance matches the distance $\overline{m}_t$ predicted by the diffusion model.

When performing kMC simulations in large domains with numerous events, it is computationally expensive to track events at the scale of individual water molecules. To improve simulation efficiency, a coarse-graining factor (c_g) is introduced to group a specified number of water molecules into one water particle. For a maximum number of water molecules n_w and a maximum number of water particles b that can exist in the volume of a voxel, the coarse-graining factor is then calculated by

$$c_g = \frac{n_w}{b+1}. \tag{18}$$

The factor c_g will be used to modify all the water diffusion rates. Equation (11) becomes

$$R_{D,w} = w \, R_{D,1}/c_g \tag{19}$$

since each water diffusion event for w water molecules in a voxel accounts for c_g number of water molecules diffusing out of the voxel.

A lattice-based kMC simulation model is developed based on the Stochastic Parallel PARticle Kinetic Simulator (SPPARKS) [49]. In this new kMC model, the molecular weight of polymer and the number of water molecules are associated with each lattice site. The water diffusion rate of each site is

calculated and updated on-the-fly based on the molecular weight and the number of water molecules onsite and those of neighboring sites.

2.3 Calibration of diffusion rates in reduced-order kMC models

In a 2D kMC model, the particles are allowed to diffuse in both dimensions. This allows the water particles to saturate or go around pores. In a 1D kMC model, water particles cannot move around pores in one-dimensional diffusion. Compared to 1D models, the number of events in 2D models can increase quadratically, which ultimately increases computational time. The dimensionality reduction method developed here is to simulate water diffusion in 2D domains efficiently with only 1D models. In a 2D domain where water diffuses in the x-direction from left to right, the 2D domain is sliced to a stack of 1D domains in the y-direction. A subset of those 1D slices is randomly selected so that 1D kMC simulation models are constructed to predict water diffusions and penetration depths corresponding to different location along the y-axis.

To perform the dimension reduction, the diffusion rates must be adjusted such that the 2D diffusion effects are captured in the 1D simulations, which is done by modifying the diffusion rates parametrically as

$$R''_{D,w} = k'_{bulk} \times R'_{D,w} \tag{20}$$
$$k'_{bulk} = A_0 + A_1\epsilon_{2D} + A_2\epsilon_{1D} \tag{21}$$
$$R''_{pore,in,w} = k'_{pore,in} \times R'_{pore,in,w} \tag{22}$$
$$k'_{pore,in} = A_3 + A_4\epsilon_{2D} + A_5\epsilon_{1D} \tag{23}$$
$$R''_{pore,out,w} = k'_{pore,out} \times R'_{pore,out,w} \tag{24}$$
$$k'_{pore,out} = A_6 + A_7\epsilon_{2D} + A_8\epsilon_{1D} \tag{25}$$

where R' are the water diffusion rates for the 2D simulations, R'' are the water diffusion rates for the 1D simulations, ϵ_{2D} and ϵ_{1D} are the porosities in the 2D and 1D simulations respectively, A's are coefficients that need to be calibrated, and k' values are non-negative scaling factor constants.

To calibrate and determine how well the 1D simulation accurately captures the 2D simulation, the distribution of the water particles after a period of time is observed. This is demonstrated in Figure 2 from 2D simulations using the calibrated k_{bulk} value from Section 3.2 where the probability of a water particle being observed at a specific penetration depth m_h at a particular time is shown. From these distributions, the statistical moments including mean ($\mu^{(1)}$), variance ($\mu^{(2)}$), and skewness ($\mu^{(3)}$) can be calculated. From the collection of 1D simulation results, a similar distribution of water particles can be obtained. Similarly, the moments $\mu^{(1)}$, $\mu^{(2)}$, and $\mu^{(3)}$ can be calculated from the 1D simulations. The calibration of 1D models can be done by minimizing the differences between these moments. The differences are quantified as the relative errors

$$E^{(p)} = \left| \frac{\mu_{2D}^{(p)} - \mu_{1D}^{(p)}}{\mu_{2D}^{(p)}} \right| \times 100\%, \ p = 1, 2, 3. \tag{26}$$

When comparison and calibration are based on multiple 2D structures, the comparison can be done based on the average error $\bar{E}$ for all structures

$$\bar{E}^{(p)} = \frac{1}{n_s} \sum_{s=1}^{n_s} E_s^{(p)}, p = 1, 2, 3 \tag{27}$$

where n_s is the number of structures for comparison. The calibration problem is to solve

$$\min_{A_0,\dots,A_8} \bar{E}^{(p)}(A_0, A_1, A_2, A_3, A_4, A_5, A_6, A_7, A_8). \tag{28}$$

so that the optimal parameters A's in Equations (21), (23), and (25) are found.
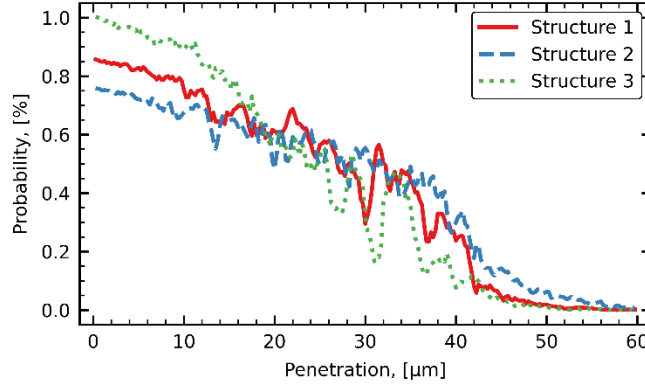

Figure 2. Distribution of water molecules after 3 seconds of diffusion based on the penetration into the material. These distributions were simulated with the 2D kMC simulations using the calibrated k_{bulk} value of 63.2%.

The calibration problem in Equation (28) lends itself to a multi-objective optimization process where the three average error functions corresponding to the three different statistical moments as the objectives need to be minimized. To accomplish this, a MOBO methodology developed by Shu *et al.* [50] with improved Pareto front quality metrics is used. The three quality metrics are the dimensional overall spread (DOS) which is a minimum hyperrectangle or bounding box of the Pareto front, the integral hyperarea difference (IHD) which integrates the area under the Pareto front by using simplexes to estimate the Pareto front, and the Gaussian hyperarea difference (GHD) which captures the overall variance of a Gaussian process model of the Pareto front. These three metrics are combined to DOS-IHD and DOS-GHD pairs and applied in two different MOBO methods. Note that the calibration method presented here is independent of multi-objective optimization approaches. Any other MOBO methods may be alternately used.

In the MOBO problem, the nine coefficients A's are the variables to be optimized and three average error functions are the objective functions. Because all final k' factors in Equations (20), (22), and (24) need to be greater than 0 and the rates cannot be negative, the lower bounds of A_0, A_3, and A_6 are 0.1 and those for other A's are 0. In addition, the upper bound of 1.5 is placed on each of A's. This is to ensure that the final k' value does not scale too high during the optimization. Allowing the rates to scale too drastically would increase the number of events and could increase computational time significantly.

3   Results and Discussions

The proposed methods for structure generation, kMC rate estimation, and reduce-order model calibration are implemented and tested.

3.1   Example Structures

A Potts model is used in SPPARKS [49] to generate a 2D structure corresponding to an image of 1000 by 150 pixels, where each pixel is a lattice site with periodicity in both directions. The Potts model simulates the phase formation and growth. Simulations are run for 500 seconds of simulation at a temperature of 0.5 electronvolts (5802 Kelvin). The post-processing tool for the images of the 2D structures is implemented in Python as described in Section 2.1. Four example PCL structures generated

following the methodology in Section 2.1 are shown in Table 1. For instance, Structure 1 falls within the range of 45% to 55% for porosity with an average pore diameter of 2.95 μm. Structure 1 is used to calibrate the water diffusion rates based on Equation (17). Structures 1, 2, and 3 will be used to calibrate the reduced-order model. Structure 4 will be used to validate the reduced-order kMC model.

PCL with the number-average molecular weight (Mn) of 80 kDa is used in all kMC simulations, where each site corresponds to a domain of 0.25 μm x 0.25 μm. Each site is either 80 kDa of material or a pore, as shown in Figure 3, to represent the two phases of the PCL microstructure. A periodic boundary condition is applied to the top and bottom boundaries of the domain along the direction of the 150 pixel height in the 2D kMC simulations. Water sources are initiated at the left boundary. The coarse-graining factor c_g is selected based on the restriction of the number of water particles per pixel to a maximum of 14, which results in $c_g = 132,485$.

Table 1. Structural properties for all four structures used in the calibration and verification.

	Porosity, [%]	Average Pore Diameter, [μm]
Structure 1	48	2.95
Structure 2	69	3.28
Structure 3	22	2.36
Structure 4	41	2.74

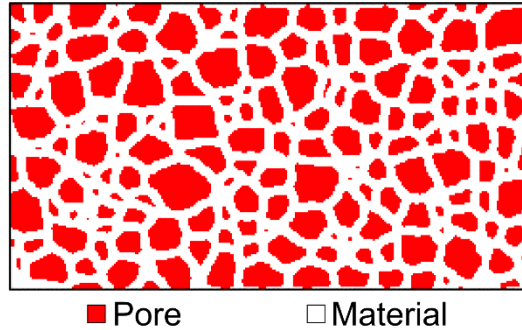

■ Pore   □ Material

Figure 3. Pore structure for Structure 1 with a porosity of 48%.

3.2   kMC Rate Calibration

The first step in the kMC rate calibration process is to determine $R'_{D,w}$ in Equation (17). This is done by selecting a diffusion coefficient D, calculating the theoretical value of $R_{D,w}$ in Equation (19), and then finding k_{bulk} in Equation (17). To find the value of k_{bulk}, a kMC simulation is run based on Structure 1. The default diffusion coefficient of water, $D = 2.299 \times 10^{-5} \, cm^2/s$ at 25 C [51], is used at the source site on the left boundary. A diffusion coefficient of 5.265 x 10^{-7} cm^2/s is used at the sites with 80 kDa [52,53]. The resultant rate $R_{D,1}$ is 1,794 s^{-1} for a cubic domain and 1,726 s^{-1} for a spherical one. Due to the increased computational time for the cubical integral, the rate for the spherical domain is used instead with the radius of the sphere calculated from Equation (15).

For Structure 1, 2D diffusion simulations with varying k_{bulk} values (100%, 70%, 60%) were executed for 4 s of physical time. Computationally it took 5 days for each simulation on a node with 24 physical processors. This translates to 120 days of computation time to simulate 4 s of physical time for each 2D kMC simulation. This computation time is dependent on the number of events that occur, which in turn is dependent on the number of water molecules in the system. The calculated mean water

This document is the unedited Author's version of a submitted work that was subsequently accepted for publication in Computational Materials Science, copyright © Elsevier.

penetration depths from the simulations with different values of k_{bulk} at different times as well as the analytical solutions of Equation (16) are compared in Table 2. In the table, the mean penetration depth in the kMC simulations ($\bar{m}_{\text{kMC}}$) is calculated as

$$\bar{m}_{\text{kMC}} = \frac{1}{n_{\text{part}}} \sum_{h=0}^{n_{\text{part}}} m_h \tag{29}$$

based on the number of water particles in the system (n_{part}). Comparing the simulation results to the analytical solutions of Equation (*16*), a simple linear interpolation is applied to the simulation results from 2 to 4 s between $k_{\text{bulk}} = 60\%$ and $k_{\text{bulk}} = 70\%$ to match the analytical solutions. By minimizing the difference, $k_{\text{bulk}} = 63.2\%$ is found as the best match to the analytical solution. Another 2D diffusion simulation for Structure 1 with the calibrated $k_{\text{bulk}} = 63.2\%$ was executed for 3 s of physical time. The mean water penetration depths from this simulation are also listed in Table 2. It is seen that the analytical solutions and simulation results for $k_{\text{bulk}} = 63.2\%$ match very well. The calibrated k_{bulk} will be used in the calibration of reduced-order models. The process of minimizing the difference between the analytical solution and 2D diffusion simulation for the mean water penetration is successful in finding the k_{bulk} value for accurate 2D kMC diffusion simulations. For this particular material, the optimal k_{bulk} value was identified quickly.

Table 2. Tabulated values for the mean water penetration ($\bar{m}_{kMC}$) for Structure 1 kMC simulations with varying k_{bulk} values compared to the analytical solution.

Time, [s]	Mean Water Penetration Depth, [µm]				
	Analytical solution of Eq. (16)	k_{bulk} 100%	k_{bulk} 70%	k_{bulk} 60%	k_{bulk} 63.2%
0.5	7.26	9.22	7.74	7.20	7.38
1.0	10.26	13.03	10.92	10.09	10.36
1.5	12.57	15.86	13.33	12.36	12.68
2.0	14.51	18.27	15.33	14.21	14.58
2.5	16.55	20.34	17.10	15.86	16.26
3.0	17.77	-	18.70	17.34	17.78
3.5	19.20	-	20.16	18.70	-
4.0	20.52	-	21.50	19.95	-

3.3 Reduced-Order kMC Model and Validation

Three 2D structures (Structures 1, 2, and 3 in Table 1) with different porosity levels are used to calibrate the reduced-order 1D kMC models based on the MOBO method. For each of the 2D structures with 1000×150 pixels, the 2D domain is decomposed to 150 slices of 1D domain along the y-direction for the 150 pixels. 10% of the slices are selected to construct 1D kMC models. This results in fifteen 1D simulations per structure. A total of forty-five 1D kMC simulations were run for each set of nine parameters ($A_0, A_1, \ldots, A_8$) that need to be calibrated. The three objective functions of errors $f_1 = \bar{E}^{(1)}$, $f_2 = \bar{E}^{(2)}$, and $f_3 = \bar{E}^{(3)}$ are minimized based on the MOBO method. All errors are calculated based on the simulation results at 3 s. Following the calibration procedure outlined in Section 2.3, both the DOS-IHD and DOS-GHD MOBO methods are applied. The optimization starts with 30 initial samples or sets of parameter values of A's. The 30 initial samples are selected using the Latin Hypercube sampling method [54,55]. Each 1D simulation is executed on its own processor to obtain a water diffusion rate. Based on Equations (20) to (25), the fifteen 1D simulations for each structure are combined and compared to their

2D structure counterparts, and the errors correspond to the objectives for optimization. In addition to the initial 30 samples, a total of 270 additional samples were obtained using each of the two MOBO methods. This results in a total of 15 and 13 Pareto solutions with the DOS-IHD and DOS-GHD methods respectively, as shown in Figure 4 (a) and Figure 4 (b). The two Pareto fronts are very similar, which suggests the consistency of the two MOBO methods. An interesting characteristic of the Pareto fronts is that they lie mostly in a narrow 2D region even in the 3D space. Therefore, the important details of the Pareto fronts can be captured by two orthogonal axes. This suggests that there is some level of dependency among the three objectives, which are based on the first three statistical moments of probability distributions.
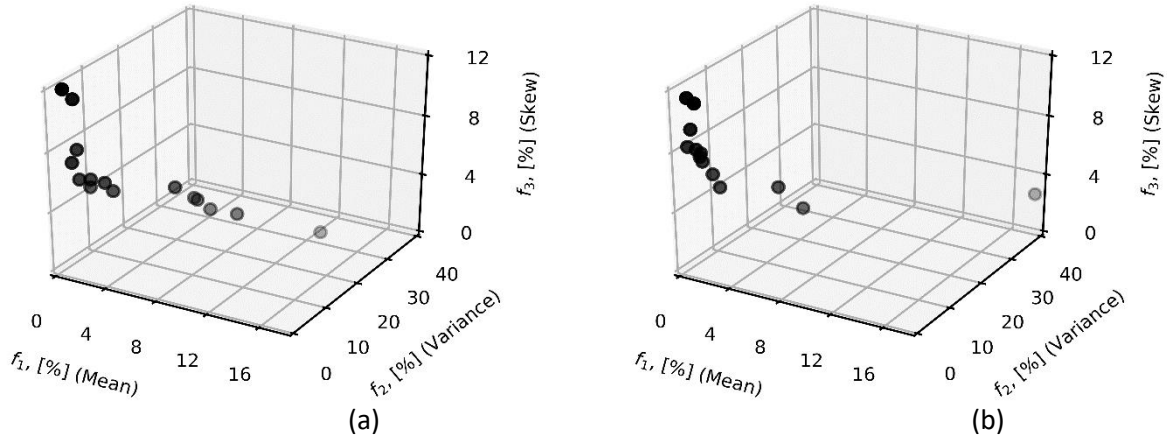

Figure 4. Plot of the Pareto fronts obtained for the (a) DOS-IHD and (b) DOS-GHD multi-objective Bayesian optimization methods.

To select the final optimal parameters A's out of the Pareto solutions, three criteria or metrics are used. The first metric is the sum of the three objectives as

$$metric_1 = f_1 + f_2 + f_3. \tag{30}$$

so that the optimal solution achieves the minimal level of error across all three moments. The second metric focuses on the variability among the three errors such that

$$metric_2 = |f_1 - f_2| + |f_2 - f_3| + |f_3 - f_1|. \tag{31}$$

The third metric combines the above two metrics as

$$metric_3 = metric_1 + metric_2. \tag{32}$$

The optimal parameters can be selected based on the minimal value of either of the above three metrics. For comparison purposes, the two smallest values in each metric from each of the two MOBO methods are selected. The results are listed in Table 3. There are some overlaps between the selected optimal parameters, which indicates the consistency among the three metrics. Therefore, only 5 optimal solutions instead of 6 were obtained with either DOS-IHD or DOS-GHD method. A total of ten reduced-order models can be constructed based on Equations (20)-(25) to obtain 1D diffusion rates from 2D diffusion rates and porosity levels. Each model includes both the 2D and 1D porosity constants, important factors in the dimensionality reduction. In the ten models, coefficients A_0, A_1, and A_2 are associated with the structure-to-structure diffusion; A_3, A_4, and A_5 are with the structure-to-pore diffusion; and A_6, A_7, and A_8 for the pore-to-structure diffusion. There are no consistent patterns within the A constants or objective solutions between the models.

Table 3. Pareto solutions which are one of the two lowest values in one of the three metrics for both the DOS-IHD and DOS-GHD method.

#	Method	A_0	A_1	A_2	A_3	A_4	A_5	A_6	A_7	A_8	f_1	f_2	f_3
1	DOS-IHD	0.79	0.29	0.61	1.50	0.36	0.29	1.28	0.70	0.52	3.22	5.08	5.33
2	DOS-IHD	0.72	0.89	0.60	0.76	0.55	0.85	0.60	0.87	0.29	1.61	4.39	5.39
3	DOS-IHD	0.91	0.44	0.39	1.10	0.39	0.88	0.74	0.61	1.02	1.53	1.78	6.28
4	DOS-IHD	1.00	0.60	0.80	1.04	0.41	0.47	0.10	0.89	1.11	2.87	4.01	5.99
5	DOS-IHD	0.86	0.82	0.33	1.50	0.77	1.08	0.95	0.97	0.63	1.20	1.08	7.43
6	DOS-GHD	0.78	0.54	0.53	1.02	0.00	1.14	0.79	1.13	0.27	2.31	3.54	5.64
7	DOS-GHD	0.83	0.67	0.28	0.89	0.56	0.85	0.75	0.64	0.75	1.84	3.30	6.46
8	DOS-GHD	1.00	0.46	0.18	0.57	0.37	1.00	0.75	0.74	0.46	1.17	1.36	8.25
9	DOS-GHD	0.99	0.51	0.42	0.61	0.56	1.00	0.48	0.94	0.51	0.29	2.03	8.17
10	DOS-GHD	0.65	0.80	0.70	1.21	0.48	0.04	0.52	1.09	0.61	5.30	9.28	5.36

To validate the reduced-order models, Structure 4 is used to perform kMC simulations. Fifteen 1D slices are selected at random from the 2D domain of Structure 4 to construct the 1D kMC models. Each of the ten Pareto solutions in Table 3 is used to construct a reduced-order 1D kMC model. From the 1D simulation results, the mean, variance, and skewness of the water distributions at the timestamps of 3 s and 4 s are obtained. They are listed in Table 4 and Table 5 respectively. The differences between these values and the ones obtained from the 2D simulation as well as the calculated three metrics are also listed in the tables.

Table 4. Information regarding the probability distributions for water penetration for structure 4 at 3 seconds.

# Time (3 s)	$\mu^{(1)}$ [um]	$\mu^{(2)}$ [um^2]	$\mu^{(3)}$	$\bar{E}^{(1)}$	$\bar{E}^{(2)}$	$\bar{E}^{(3)}$	metric_1	metric_2	metric_3
2D Simulation	16.36	126.58	0.50	-	-	-	-	-	-
1D Model 1	16.34	125.30	0.54	0.14	1.02	8.76	9.92	17.24	27.16
1D Model 2	16.09	123.12	0.54	1.66	2.73	8.11	12.50	12.91	25.41
1D Model 3	16.36	126.64	0.53	0.00	0.05	6.87	6.92	13.72	20.64
1D Model 4	16.36	130.68	0.56	0.03	3.24	12.07	15.34	24.08	39.42
1D Model 5	16.44	127.63	0.52	0.47	0.83	5.09	6.38	9.24	15.62
1D Model 6	16.25	124.57	0.55	0.67	1.59	10.10	12.36	18.84	31.20
1D Model 7	16.13	122.02	0.53	1.43	3.60	6.66	11.69	10.45	22.14
1D Model 8	16.53	129.37	0.55	0.99	2.20	10.69	13.88	19.39	33.27
1D Model 9	16.39	128.04	0.54	0.14	1.15	8.96	10.25	17.63	27.88
1D Model 10	16.12	123.65	0.56	1.51	2.32	11.24	15.07	19.46	34.53

Table 5. Information regarding the probability distributions for water penetration for structure 4 at 4 seconds.

# Time (4 s)	$\mu^{(1)}$ [um]	$\mu^{(2)}$ [um^2]	$\mu^{(3)}$	$\bar{E}^{(1)}$	$\bar{E}^{(2)}$	$\bar{E}^{(3)}$	metric$_1$	metric$_2$	metric$_3$
2D Simulation	18.97	170.21	0.50	-	-	-	-	-	-
1D Model 1	18.97	167.11	0.51	0.04	1.82	2.86	4.72	5.65	10.37
1D Model 2	18.60	163.93	0.52	1.92	3.69	4.71	10.32	5.59	15.91
1D Model 3	18.97	169.42	0.51	0.00	0.47	1.81	2.28	3.61	5.89
1D Model 4	18.83	169.56	0.52	0.75	0.39	5.71	6.85	10.66	17.50
1D Model 5	19.06	170.57	0.50	0.50	0.21	1.25	1.96	2.09	4.04
1D Model 6	18.84	167.02	0.51	0.65	1.87	3.28	5.80	5.25	11.05
1D Model 7	18.69	164.52	0.51	1.46	3.34	3.32	8.12	3.76	11.88
1D Model 8	19.14	172.99	0.53	0.91	1.63	7.40	9.94	12.97	22.92
1D Model 9	19.00	172.31	0.52	0.19	1.23	5.20	6.62	10.01	16.63
1D Model 10	18.64	164.38	0.52	1.75	3.42	5.44	10.61	7.39	17.99

It is seen that every model has very small errors for $\mu^{(1)}$ and $\mu^{(2)}$. The maximum error is 3.69%. Models 3 and 5 have the lowest errors for $\mu^{(3)}$. Models 6 and 7 performed the best among all DOS-GHD models based on the proposed evaluation metrics. Overall, the DOS-IHD models performed better with lower overall objectives and metrics.

As an illustration, the results from Model 5 are shown as follows. The water distributions at the timestamp of 3 s from the 2D and 1D simulations are compared visually in Figure 5 (a). The 1D simulations are visualized using 1D strips overlaid onto the 2D simulation. There is little difference between the 1D strips and the 2D simulation in the region that is close to the water source. At the penetration depth of approximately 30 μm, some small discrepancies within some pores or in the solid areas between pores are observed. Overall, the 1D strips show very similar trends to the 2D simulation. To compare the results quantitatively between the 2D and 1D simulations, the water concentrations at different penetration depths for 3 s and 4 s are shown in Figure 5 (b) and (c) respectively. There is strong agreement between the 2D and 1D simulations water distributions suggesting that the 1D model accurately represents the system. The 1D model even captures irregularities, such as the dip of concentration that occurs at approximately 30 μm in both 2D and 1D simulations. This dip is due to a lack of pores in the region since pores would capture more water particles. The 1D simulation successfully captures the expected dip from the 2D simulation. Even though small discrepancies between the 1D and 2D simulations are observed in Figure 5 (a), there are enough 1D slices such that the accumulation of all slices accurately predict the water penetration statistically. The gain of computational efficiency comes at the cost of losing some information in the second dimension. Nevertheless, this is appropriate for the applications when the 1D diffusion of molecules dominates.

To further examine the 1D kMC model, Model 5 was further run until the timestamp of 180 s was reached. The predicted average penetration depth is compared with the analytical calculation from Equation (16) as shown in Figure 6. Since the simulation domain has a maximum width of 1,000 pixels, which is equivalent to 250 μm, the maximum average penetration depth is 125 μm. After water molecules reach the far edge of the simulation domain, which occurs only after a few seconds, the average penetration depth of the water would approach the maximum of 125 μm. The simulation average penetration depth will approach the maximum average at a slightly slower rate than the analytical

calculation due to the simulation domain. These trends are observed in Figure 6, suggesting that the prediction from the reduced-order model is accurate.

To simulate water diffusion for 4 s and 180 s, 1D kMC model took 1 and 8 hours respectively with 15 processors for a total of 15 and 120 hours of computation time respectively. The 2D kMC model took 5 days with 24 processors to simulate the process of 4 s for a total of 2,880 hours of computation time. It is estimated that it would take over 225 days to run the 2D simulation for 180 s of diffusion with a total of 129,600 hours of computation time. The dimensionality reduction results in a 675-fold speedup. This efficiency improvement comes from the significant reduction of diffusion events.

(a)

(b)

(c)
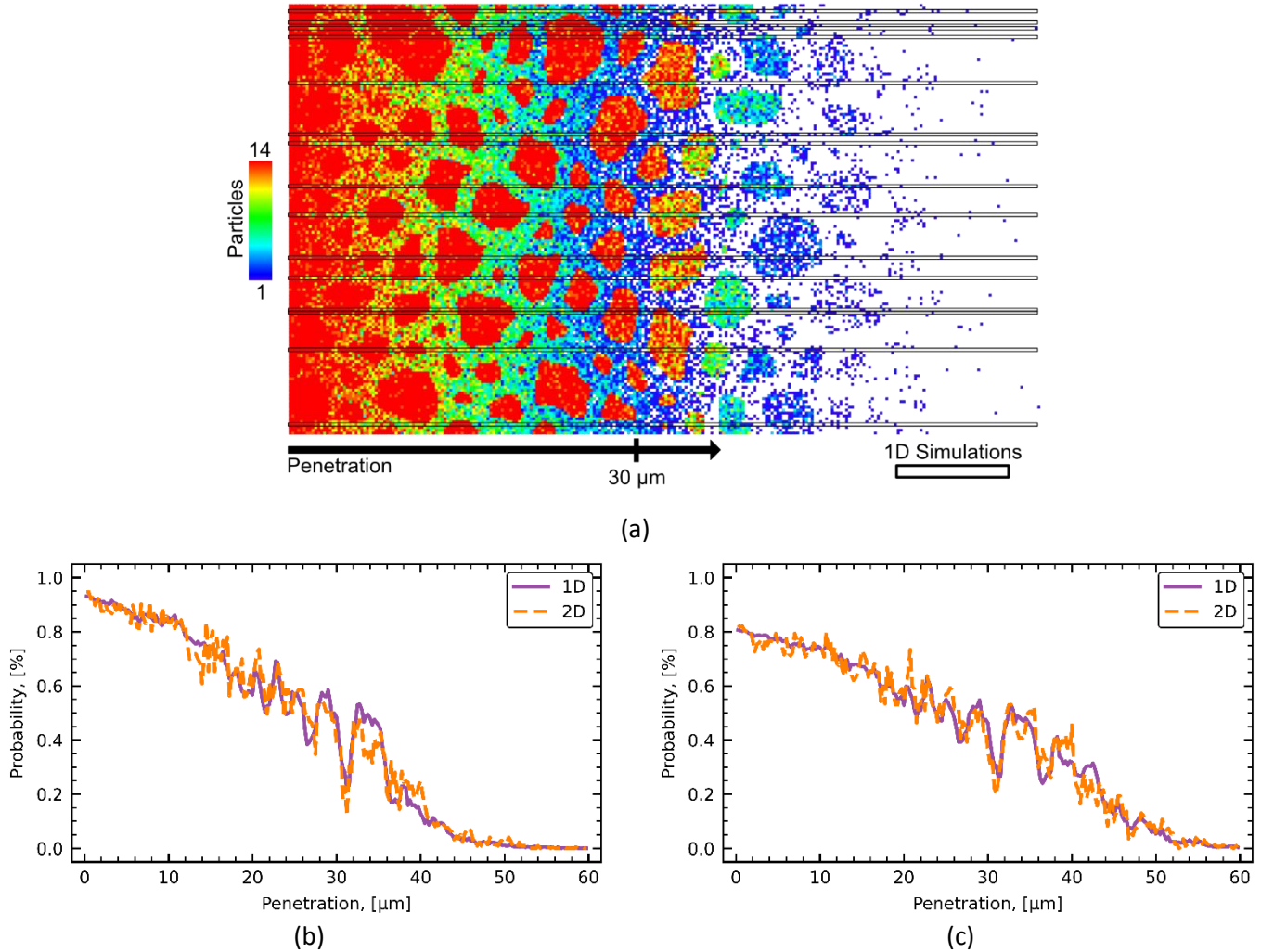
Figure 5. Structure 4 comparison between the 2D simulation and Model 5 simulation. (a) Shows a visual comparison of the water particles at 3 s. The probability distributions of the water particles for the 2D and Model 5 are shown at (b) 3 s and (c) 4 s.
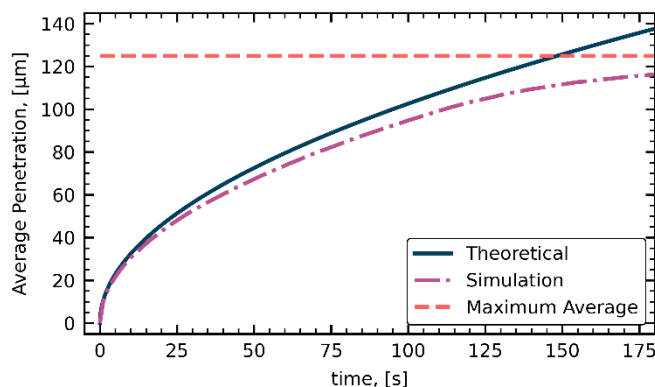
Figure 6. Average penetration for the 1D simulations of structure 4 using model 5 compared to the theoretical average penetration and the maximum possible for structure 4.

3.4   Limitations and Future Improvements

The proposed dimensionality reduction approach only works for one-dimensional diffusion, where diffusion predominately occurs along one axis. This approach would likely fail if diffusions occur along two or more axes. This approach also requires costly high-dimensional simulations to be performed to calibrate the reduced-order model. Running high-dimensional simulations with simpler or smaller structures at a shorter timescale can alleviate the computational burden. Yet extrapolation can potentially lead to large prediction errors.

In this work, dimensionality reduction is achieved by randomly sampling 1D domains from the 2D region. The reduction becomes less efficient when defects are present non-uniformly in the material structure. To accurately capture the effects of non-uniform defects, a larger number of samples and reduced-order simulations may be required. How to choose representative samples for a balance of efficiency and accuracy becomes a major research question. The related question is how to identify the non-uniformity of the defects. The identification can be done with image processing techniques. A higher percentage of samples can be allocated specifically to the region with denser defects. The sampling scheme itself becomes an important research topic. The model calibration procedure needs to be integrated with the sampling scheme.

If the kMC rates are not calibrated with actual structures for specific applications, the simulation predictions can be unreliable. The rates can be time- and location-dependent, instead of as constants. For biodegradable scaffolds, physiological conditions can impact the material properties thus the diffusion. For instance, the static or dynamic forces that the biodegradable scaffolds undergo inside the body [56] can stretch or compress the structures. As a result, the configuration of the polymer chains can change, directly affecting the diffusion rates, which can be studied via molecular dynamics [52]. In addition, the effects of hydrolysis on the diffusion rates need to be analyzed. The direct kMC simulation of the coupled reaction-diffusion process will suffer from the issue of time scale difference. The problem may be alleviated using sequential kMC simulations to separate these two types of events, or by incorporating time-dependent rates [57–59] into a single kMC simulation. Furthermore, similar to other kMC acceleration methods, the reduced-order modeling approach introduces errors and the uncertainty needs to be quantified [58]. In general, the accuracy of kMC simulation predictions remains the major research issue.

15

4 Summary and conclusions

This paper outlines a dimensionality reduction technique for kMC simulations to accelerate the simulation of diffusion. By reducing the simulation domain from 2D to 1D and carefully calibrating the model parameters, a 675-fold speedup can be achieved without losing much fidelity and accuracy of simulation predictions. A MOBO method is developed to calibrate the parameters of reduced-order models with the considerations of several target properties comprehensively. A new way to generate 2D porous microstructures is also developed where phases are formed aided by a Potts model. The developed technique is applied to water diffusion, and it is seen that water diffusion in 2D porous PCL structures can be effectively simulated with several 1D kMC models. It is postulated that the same methodology may be applied to reduce a 3D model to 1D if the diffusion direction is predominately in one direction.

5 Declaration of Competing Interest

The authors declare no known competing interests that bias this work.

6 CRediT authorship contribution statement

Jesse M. Sestito: Data curation, Formal analysis, Investigation, Methodology, Visualization, Software, Writing – review & editing. **Tequila A. L. Harris:** Writing – review & editing, Conceptualization, Methodology. **Yan Wang:** Funding acquisition, Writing – review & editing, Conceptualization, Resources, Methodology.

7 Acknowledgements

8 Data Availability

The raw/processed data required to reproduce these findings cannot be shared at this time due to technical or time limitations.

9 References

[1]   S. Bose, S. Vahabzadeh, A. Bandyopadhyay, Bone tissue engineering using 3D printing, Mater. Today. 16 (2013) 496–504. https://doi.org/10.1016/j.mattod.2013.11.017.

[2]   X. Han, L. Ding, Y. Wang, J. Pan, C. Sinka, A phenomenological model for the degradation of biodegradable polymers, Biomaterials. 29 (2008) 3393–3401. https://doi.org/10.1016/j.biomaterials.2008.04.042.

[3]   T. Zhang, S. Zhou, X. Gao, Z. Yang, L. Sun, D. Zhang, A multi-scale method for modeling degradation of bioresorbable polyesters, Acta Biomater. 50 (2017) 462–475. https://doi.org/10.1016/j.actbio.2016.12.046.

[4]   S.S. Joshi, A.M. Mebel, Computational modeling of biodegradable blends of starch amylose and poly-propylene carbonate, Polymer (Guildf). 48 (2007) 3893–3901. https://doi.org/10.1016/j.polymer.2007.04.059.

[5]   M. Entrialgo-Castaño, A.E. Salvucci, A. Lendlein, D. Hofmann, An atomistic modeling and

quantum mechanical approach to the hydrolytic degradation of aliphatic polyesters, Macromol. Symp. 269 (2008) 47–64. https://doi.org/10.1002/masy.200850908.

[6]   Y. Chen, S. Zhou, Q. Li, Mathematical modeling of degradation for bulk-erosive polymers: Applications in tissue engineering scaffolds and drug delivery systems, Acta Biomater. 7 (2011) 1140–1149. https://doi.org/10.1016/j.actbio.2010.09.038.

[7]   A.G. J. Siepmann, Mathematical modeling of bioerodible, polymeric drug delivery systems, Adv. Drug Deliv. Rev. 48 (2000) 229–247. https://doi.org/10.1080/01430750.2017.1324812.

[8]   D. Hofmann, M. Entrialgo-Castaño, K. Kratz, A. Lendlein, Knowledge-based approach towards hydrolytic degradation of polymer-based biomaterials, Adv. Mater. 21 (2009) 3237–3245. https://doi.org/10.1002/adma.200802213.

[9]   H. Samami, J. Pan, A constitutive law for degrading bioresorbable polymers, J. Mech. Behav. Biomed. Mater. 59 (2016) 430–445. https://doi.org/10.1016/j.jmbbm.2016.02.026.

[10]   J. Coffel, S. Gandhi, E. Nuxoll, Unified polymer erosion model for pulsatile drug delivery, J. Memb. Sci. 512 (2016) 61–72. https://doi.org/10.1016/j.memsci.2016.03.055.

[11]   K. Sevim, J. Pan, A model for hydrolytic degradation and erosion of biodegradable polymers, Acta Biomater. 66 (2018) 192–199. https://doi.org/10.1016/j.actbio.2017.11.023.

[12]   J. Siepmann, N. Faisant, J. Benoit, A New Mathematical Model Quantifying Drug Release from Bioerodible Microparticles Using Monte Carlo Simulations, Pharm. Res. 19 (2002) 1885–1893. https://doi.org/10.1023/A:1021457911533.

[13]   Y. Mohammadi, E. Jabbari, Monte Carlo simulation of degradation of porous poly(lactide) scaffolds, 1 effect of porosity on pH, Macromol. Theory Simulations. 15 (2006) 643–653. https://doi.org/10.1002/mats.200600036.

[14]   X. Han, J. Pan, Polymer chain scission, oligomer production and diffusion: A two-scale model for degradation of bioresorbable polyesters, Acta Biomater. 7 (2011) 538–547. https://doi.org/10.1016/j.actbio.2010.09.005.

[15]   M. Andersen, C. Panosetti, K. Reuter, A Practical Guide to Surface Kinetic Monte Carlo Simulations, Front. Chem. 7 (2019) 1–24. https://doi.org/10.3389/fchem.2019.00202.

[16]   S. Neumeier, H.U. Rehman, J. Neuner, C.H. Zenk, S. Michel, S. Schuwalow, J. Rogal, R. Drautz, M. Göken, Diffusion of solutes in fcc Cobalt investigated by diffusion couples and first principles kinetic Monte Carlo, Acta Mater. 106 (2016) 304–312. https://doi.org/10.1016/j.actamat.2016.01.028.

[17]   S. Sakong, A.K. Henß, J. Wintterlin, A. Groß, Diffusion on a Crowded Surface: kMC Simulations, J. Phys. Chem. C. 124 (2020) 15216–15224. https://doi.org/10.1021/acs.jpcc.0c03042.

[18]   B. Maté, S. Cazaux, M.Á. Satorre, G. Molpeceres, J. Ortigoso, C. Millán, C. Santonja, Diffusion of CH4 in amorphous solid water, Astron. Astrophys. 643 (2020) 1–14. https://doi.org/10.1051/0004-6361/202038705.

[19]   I.D. Luzhansky, A.D. Schwartz, J.D. Cohen, J.P. Macmunn, L.E. Barney, L.E. Jansen, S.R. Peyton, Anomalously diffusing and persistently migrating cells in 2D and 3D culture environments, APL Bioeng. 2 (2018). https://doi.org/10.1063/1.5019196.

[20]   K. Muralidharan, P. Deymier, M. Stimpfl, N.H. de Leeuw, M.J. Drake, Origin of water in the inner Solar System: A kinetic Monte Carlo study of water adsorption on forsterite, Icarus. 198 (2008) 400–407. https://doi.org/10.1016/j.icarus.2008.07.017.

[21]   Z. Zheng, R.M. Stephens, R.D. Braatz, R.C. Alkire, L.R. Petzold, A hybrid multiscale kinetic Monte Carlo method for simulation of copper electrodeposition, J. Comput. Phys. 227 (2008) 5184–5199. https://doi.org/10.1016/j.jcp.2008.01.056.

[22]   E. Rusli, T.O. Drews, D.L. Ma, R.C. Alkire, R.D. Braatz, Robust nonlinear feedback-feedforward control of a coupled kinetic Monte Carlo-finite difference simulation, J. Process Control. 16 (2006) 409–417. https://doi.org/10.1016/j.jprocont.2005.05.007.

[23]   Y. Lou, P.D. Christofides, Estimation and control of surface roughness in thin film growth using kinetic Monte-Carlo models, Chem. Eng. Sci. 58 (2003) 3115–3129. https://doi.org/10.1016/S0009-2509(03)00166-0.

[24]   C.I. Siettos, A. Armaou, A.G. Makeev, I.G. Kevrekidis, Microscopic/stochastic timesteppers and coarse control: a kinetic Monte Carlo example, AIChE J. 49 (2002) 1922–1926. http://arxiv.org/abs/nlin/0207017.

[25]   A. Hashemi, M. Núñez, P. Plecháč, D.G. Vlachos, Stochastic averaging and sensitivity analysis for two scale reaction networks, J. Chem. Phys. 144 (2016). https://doi.org/10.1063/1.4942008.

[26]   D.T. Gillespie, A general method for numerically simulating the stochastic time evolution of coupled chemical reactions, J. Comput. Phys. 22 (1976) 403–434. https://doi.org/10.1016/0021-9991(76)90041-3.

[27]   M. Rathinam, L.R. Petzold, Y. Cao, D.T. Gillespie, Stiffness in stochastic chemically reacting systems: The implicit tau-leaping method, J. Chem. Phys. 119 (2003) 12784–12794. https://doi.org/10.1063/1.1627296.

[28]   E.L. Haseltine, J.B. Rawlings, Approximate simulation of coupled fast and slow reactions for stochastic chemical kinetics, J. Chem. Phys. 117 (2002) 6959–6969. https://doi.org/10.1063/1.1505860.

[29]   W. E, D. Liu, E. Vanden-Eijnden, Nested stochastic simulation algorithms for chemical kinetic systems with multiple time scales, J. Comput. Phys. 221 (2007) 158–180. https://doi.org/10.1016/j.jcp.2006.06.019.

[30]   M.A. Katsoulakis, A.J. Majda, D.G. Vlachos, Coarse-grained stochastic processes for microscopic lattice systems, Proc. Natl. Acad. Sci. U. S. A. 100 (2003) 782–787. https://doi.org/10.1073/pnas.242741499.

[31]   J. Deng, D. Morgan, I. Szlufarska, Kinetic Monte Carlo simulation of the effective diffusivity in grain boundary networks, Comput. Mater. Sci. 93 (2014) 36–45. https://doi.org/10.1016/j.commatsci.2014.06.028.

[32]   S. Collins, M. Stamatakis, D.G. Vlachos, Adaptive coarse-grained Monte Carlo simulation of reaction and diffusion dynamics in heterogeneous plasma membranes, BMC Bioinformatics. 11 (2010) 218. https://doi.org/10.1186/1471-2105-11-218.

[33]   A.G. Makeev, D. Maroudas, I.G. Kevrekidis, "Coarse" stability and bifurcation analysis using stochastic simulators: Kinetic Monte Carlo examples, J. Chem. Phys. 116 (2002) 10083–10091.

https://doi.org/10.1063/1.1476929.

[34]   J.W. Kim, K.H. Shin, Y.H. Koh, M.J. Hah, J. Moon, H.E. Kim, Production of poly(ε-
caprolactone)/hydroxyapatite composite scaffolds with a tailored macro/micro-porous structure,
high mechanical properties, and excellent bioactivity, Materials (Basel). 10 (2017).
https://doi.org/10.3390/ma10101123.

[35]   V. Guarino, F. Causa, L. Ambrosio, Porosity and mechanical properties relationship in PCL porous
scaffolds, J. Appl. Biomater. Biomech. 5 (2007) 149–157.
https://doi.org/10.1177/228080000700500303.

[36]   T. Kouya, S.I. Tada, H. Minbu, Y. Nakajima, M. Horimizu, T. Kawase, D.R. Lloyd, T. Tanaka,
Microporous membranes of PLLA/PCL blends for periosteal tissue scaffold, Mater. Lett. 95 (2013)
103–106. https://doi.org/10.1016/j.matlet.2012.12.076.

[37]   U. Gómez-Pinedo, L. Sanchez-Rojas, S. Vidueira, F.J. Sancho, C. Martínez-Ramos, M. Lebourg, M.
Monleón Pradas, J.A. Barcia, Bridges of biomaterials promote nigrostriatal pathway regeneration,
J. Biomed. Mater. Res. - Part B Appl. Biomater. 107 (2019) 190–196.
https://doi.org/10.1002/jbm.b.34110.

[38]   M. Abedalwafa, L. Chao-jing, W. Fu-jun, W. Lu, L. Ming-qiang, J. Hao, Mechanical Properties of
Poly(ε-caprolactone)/Polyethylene Terephthalate Composite Prototype Small Diameter Vascular
Graft, Proc. 2012 Int. Forum Biomed. Text. Mater. Shanghai, China. (2012) 132–137.

[39]   C.E. Nyitray, R. Chang, G. Faleo, K.D. Lance, D.A. Bernards, Q. Tang, T.A. Desai, Polycaprolactone
Thin-Film Micro- and Nanoporous Cell-Encapsulation Devices, ACS Nano. 9 (2015) 5675–5682.
https://doi.org/10.1021/acsnano.5b00679.

[40]   T. Oppelstrup, V. V Bulatov, A. Donev, M.H. Kalos, G.H. Gilmer, B. Sadigh, First-passage kinetic
Monte Carlo method, Phys. Rev. E. Stat. Nonlin. Soft Matter Phys. 80 (2009) 66701.

[41]   A.J. Mauro, J.K. Sigurdsson, J. Shrake, P.J. Atzberger, S.A. Isaacson, A First-Passage Kinetic Monte
Carlo method for reaction-drift-diffusion processes, J. Comput. Phys. 259 (2014) 536–567.
https://doi.org/10.1016/j.jcp.2013.12.023.

[42]   T. Opplestrup, V. V. Bulatov, G.H. Gilmer, M.H. Kalos, B. Sadigh, First-Passage Monte Carlo
Algorithm: Diffusion without All the Hops, Phys. Rev. Lett. 97 (2006) 230602.
https://doi.org/10.1103/PhysRevLett.97.230602.

[43]   A. Donev, V. V. Bulatov, T. Oppelstrup, G.H. Gilmer, B. Sadigh, M.H. Kalos, A First-Passage Kinetic
Monte Carlo algorithm for complex diffusion-reaction systems, J. Comput. Phys. 229 (2010)
3214–3236. https://doi.org/10.1016/j.jcp.2009.12.038.

[44]   J. Crank, The mathematics of diffusion, Oxford university press, 1979.

[45]   J. Wand, T. Hou, Application of Molecular Dynamics Simulations in Molecular Property Prediction
II: Diffusion Coefficient, J. Comput. Chem. 32 (2012) 3505–3519.
https://doi.org/10.1002/jcc.21939.Application.

[46]   Y. Ohya, K. Nagahama, Biodegradable polymeric materials, Drug Deliv. Syst. 23 (2008) 618–626.
https://doi.org/10.2745/dds.23.618.

[47]   F. Xu, M. Wei, X. Zhang, Y. Song, W. Zhou, Y. Wang, How Pore Hydrophilicity Influences Water

Permeability?, Research. 2019 (2019) 1–10. https://doi.org/10.34133/2019/2581241.

[48]   K. Seidenberger, F. Wilhelm, T. Schmitt, W. Lehnert, J. Scholta, Estimation of water distribution and degradation mechanisms in polymer electrolyte membrane fuel cell gas diffusion layers using a 3D Monte Carlo model, J. Power Sources. 196 (2011) 5317–5324. https://doi.org/10.1016/j.jpowsour.2010.08.068.

[49]   C. Garcia Cardona, G. Wagner, V. Tikare, E. Holm, S. Plimpton, A. Thompson, A. Slepoy, X. Zhou, C. Battaile, M. Chandross, Crossing the mesoscale no-man<U+2019>s land via parallel kinetic Monte Carlo., Albuquerque, NM, and Livermore, CA (United States), 2009. https://doi.org/10.2172/966942.

[50]   L. Shu, P. Jiang, X. Shao, Y. Wang, A New Multi-Objective Bayesian Optimization Formulation With the Acquisition Function for Convergence and Diversity, J. Mech. Des. 142 (2020) 1–10. https://doi.org/10.1115/1.4046508.

[51]   M. Holz, S.R. Heil, A. Sacco, Temperature-dependent self-diffusion coefficients of water and six selected molecular liquids for calibration in accurate 1H NMR PFG measurements, Phys. Chem. Chem. Phys. 2 (2000) 4740–4742. https://doi.org/10.1039/b005319h.

[52]   J.M. Sestito, M.L. Thatcher, L. Shu, T.A.L. Harris, Y. Wang, Coarse-Grained Force Field Calibration Based on Multiobjective Bayesian Optimization to Simulate Water Diffusion in Poly-ϵ-caprolactone, J. Phys. Chem. A. 124 (2020) 5042–5052. https://doi.org/10.1021/acs.jpca.0c01939.

[53]   M. Galizia, P. La Manna, G. Mensitieri, M. Pannico, P. Musto, Diffusion in polymers as investigated by two-dimensional correlation spectroscopy: The H2O/PCL system, J. Mol. Struct. 1069 (2014) 290–298. https://doi.org/10.1016/j.molstruc.2014.02.045.

[54]   J. Park, Optimal Latin-hypercube designs for computer experiments, J. Stat. Plan. Inference. 39 (1994) 95–111. https://doi.org/10.1016/0378-3758(94)90115-5.

[55]   G.G. Wang, Adaptive response surface method using inherited Latin hypercube design points, J. Mech. Des. Trans. ASME. 125 (2003) 210–220. https://doi.org/10.1115/1.1561044.

[56]   A.R. Knutsen, S.L. Borkowski, E. Ebramzadeh, C.L. Flanagan, S.J. Hollister, S.N. Sangiorgio, Static and dynamic fatigue behavior of topology designed and conventional 3D printed bioresorbable PCL cervical interbody fusion devices, J. Mech. Behav. Biomed. Mater. 49 (2015) 332–342. https://doi.org/10.1016/j.jmbbm.2015.05.015.

[57]   S. Schnell, T.E. Turner, Reaction kinetics in intracellular environments with macromolecular crowding: Simulations and rate laws, Prog. Biophys. Mol. Biol. 85 (2004) 235–260. https://doi.org/10.1016/j.pbiomolbio.2004.01.012.

[58]   Y. Wang, Reliable kinetic Monte Carlo simulation based on random set sampling, Soft Comput. 17 (2013) 1439–1451. https://doi.org/10.1007/s00500-013-1013-y.

[59]   A.P.J. Jansen, Monte Carlo simulations of chemical reactions on a surface with time-dependent reaction-rate constants, Comput. Phys. Commun. 86 (1995) 1–12. https://doi.org/10.1016/0010-4655(94)00155-U.